Number of words = 6787

FULL PAPER

SPARKLING: variable-density k-space filling curves for accelerated T2*-weighted MRI.

Carole Lazarus[1,2,3] | **Pierre Weiss**[4,5,6] | **Nicolas Chauffert**[1,2,3] | **Franck Mauconduit**[7] | **Loubna El Gueddari**[1,2,3] | **Christophe Destrieux**[8] | **Ilyess Zemmoura**[8] | **Alexandre Vignaud**[1,2] | **Philippe Ciuciu**[1,2,3]

[1]NeuroSpin, CEA Saclay, 91191 Gif-sur-Yvette cedex, France

[2]Université Paris-Saclay, France

[3]Parietal, INRIA, 91120 Palaiseau, France

[4]ITAV USR3505 CNRS, 31000 Toulouse, France

[5]IMT UMR 5219 CNRS, 31400 Toulouse, France

[6]Université de Toulouse, France

[7]Siemens Healthineers, 93210 Saint-Denis, France

[8]Université François-Rabelais de Tours, INSERM, Imagerie et Cerveau UMR 930, 37000 Tours, France

Correspondence
Philippe Ciuciu PhD, NeuroSpin, CEA, Gif-sur-Yvette, 91191, France
Email: philippe.ciuciu@cea.fr

Funding information

Purpose: To present a new optimization-driven design of optimal k-space trajectories in the context of compressed sensing: Spreading Projection Algorithm for Rapid K-space sampLING (SPARKLING).

Theory: The SPARKLING algorithm is a versatile method inspired from stippling techniques that automatically generates optimized sampling patterns compatible with MR hardware constraints on maximum gradient amplitude and slew rate. These non-Cartesian sampling curves are designed to comply with key criteria for optimal sampling: a controlled distribution of samples (e.g., variable density) and a locally uniform k-space coverage.

Methods: *Ex vivo* and *in vivo* prospective T_2^*-weighted acquisitions were performed on a 7 Tesla scanner using the SPARKLING trajectories for various setups and target densities. Our method was compared to radial and variable-density spiral trajectories for high resolution imaging.

Results: Combining sampling efficiency with compressed sensing, the proposed sampling patterns allowed up to 20-fold reductions in MR scan time (compared to fully-sampled Cartesian acquisitions) for two-dimensional T_2^*-weighted imaging without deterioration of image quality, as demonstrated by our experimental results at 7 Tesla on *in vivo* human brains for a high in-plane resolution of 390 μm. In comparison to existing non-Cartesian sampling strategies, the proposed technique also yielded superior image quality.

Conclusion: The proposed optimization-driven design of k-space trajectories is a versatile framework that is able to enhance MR sampling performance in the context of compressed sensing.

KEYWORDS

Compressed Sensing, k-space trajectories, optimization, variable density

| INTRODUCTION

Magnetic resonance imaging (MRI) is one of the most powerful and safest imaging modalities for examining the human body. High-resolution MRI is expected to aid in the understanding and diagnosis of many neurodegenerative pathologies involving submillimetric lesions or morphological changes, such as Alzheimer's disease and multiple sclerosis [1, 2, 3]. Although high-magnetic-field systems can deliver a sufficient signal-to-noise ratio (SNR) to increase spatial resolution [4], long scan times and motion sensitivity continue hindering the utilization of high resolution MRI. Despite the development of corrections for bulk and physiological motion [5, 6, 7, 8], long acquisition times remain a major obstacle to high-resolution acquisition, especially in clinical applications.

In MRI, an image is acquired indirectly through its Fourier transform, which represents its spatial frequency content. More precisely, the Fourier domain, referred to as the *k-space*, is sampled along parameterized curves generated by varying magnetic field gradients. Owing to hardware and physiological constraints (e.g., peripheral nerve stimulations), these encoding gradients have a bounded amplitude and a maximum slew rate, imposing limitations of speed and acceleration on the sampling trajectories. In addition, the rapid decay of the MR signal prevents the measurement of all the needed data at once. For these reasons, MR sampling is generally performed sequentially using segmented sampling patterns composed of multiple shots. Filling the entire k-space array may thus require a long imaging time especially for high-resolution imaging. In this work, we make significant progress in accelerating the time of segmented MR acquisitions with minimum deterioration of image quality, by limiting the number of shots using optimized sampling patterns. The proposed strategy can be used in combination with parallel imaging [9, 10], yielding even more important acceleration factors.

Most MRI sampling methods are currently based on the Shannon-Nyquist theory, which relies on the use of Cartesian sampling, with the number of required samples increasing with the resolution. The newly developed theory of compressed sensing [11, 12, 13] offers a promising solution for reducing the MRI scan time, since it theoretically allows for subsampling of the k-space while guaranteeing exact reconstructions. While early theoretical results were based on concepts such as incoherence or restricted isometry properties, more recent developments [14, 15] suggest compliance with two criteria for optimal sampling:

(i) The sampling pattern should be distributed along a given variable density. In the case of MRI, low frequencies should be sampled more densely than high frequencies.
(ii) Coverage of the k-space should be locally uniform to avoid large gaps and clusters of samples.

Although seemingly unrelated, the Shannon-Nyquist and compressive sampling theories advocate for the same criteria since both methods promote *locally uniform sampling patterns* and differ only in the target density (uniform density for the Shannon-Nyquist theory and variable density for compressed sensing theory). Methods to generate point configurations satisfying (i) and (ii) have been extensively studied in computer graphics and range from simple dart throwing to Poisson disk sampling or more elaborate optimal transportation-based techniques [16, 17]. Nevertheless, since they do not account for hardware constraints and produce discontinuous samples, these algorithms are unable to provide sampling curves for MRI.

This limitation may explain why the 2D sampling patterns used in practice are essentially made of simple analytical models such as Cartesian lines [18, 19], non-Cartesian radial spokes [20, 21, 22], spiral interleaves [23, 24] and variations of these patterns [25, 26, 27, 28, 29]. Although these geometrical curves may enable relatively rapid scanning, they do not take advantage of all the degrees of freedom offered by the hardware and lack flexibility to comply with the above optimal criteria. They may therefore be further improved to reduce MRI scan time.

Here, we explore the feasibility and improve a method introduced recently in [15], that may overcome these limitations by taking a radically new approach to the design of k-space sampling. The acronym of this approach is SPARKLING for Spreading Projection Algorithm for Rapid K-space sampLING. The method relies on optimization to generate k-space trajectories complying with criteria (i)-(ii) under the hardware constraints. A tailored distance between the sample distribution and a prescribed density is minimized with a projected gradient descent. In this work, we accelerate the algorithm by one order of magnitude by choosing the step size based on a Barzilai-Borwein strategy [30]. Moreover, we suggest to use our algorithm with highly-sampled trajectories in the same manner as for spiral imaging [31]. This has the double advantage of improving the sampling efficiency by maximizing the k-space coverage per unit time, and to mitigate the side-effects of the ADC filters [32].

The proposed sampling patterns were prospectively validated both *ex vivo* and *in vivo* in healthy volunteers on a 7 Tesla MR scanner for T_2^*-weighted imaging. The versatility of the method was demonstrated for various setups and target densities. In comparison to standard fully-sampled Cartesian acquisitions, our strategy significantly reduced the scan time while maintaining good image quality. Moreover, SPARKLING-generated acquisitions were compared to acquisitions obtained with two non-Cartesian sampling methods widely used in anatomical MRI, namely, radial and spiral trajectories. Using the same equally accelerated gradient echo sequence (GRE) and without additional equipment, we show that our method achieves enhanced image quality. The stability of SPARKLING-generated acquisitions was also tested for very high in-plane acceleration factors of up to 20. We chose a T_2^* contrast for their clinical interest at 7 Tesla but also because they allow long readouts which are favorable to highly circumvoluted SPARKLING trajectories. Nevertheless, these trajectories may be deployed for other contrasts such as T_1 with a lower expected acceleration factor.

| THEORY

In this section, we present the SPARKLING algorithm, which is based on the theoretical works presented in [33, 34, 15]. The key idea is to optimize the samples location in the non-Cartesian k-space, in order to follow criteria (i)-(ii), while respecting the gradient hardware constraints and additional linear constraints such as passage through the origin of the k-space at a given time (the *echo time*), which is crucial for controlling the image contrast. Moreover, when using compressed sensing, since the selection of the target density proved to be important for optimal results, we incorporated in our method a density generator that adapts to the resolution and the number of samples.

| Optimizing the sampling pattern

A k-space trajectory is usually composed of several segments $\boldsymbol{k}(t)$, also referred to as shots, which are controlled by magnetic field gradients $G(\tau)$ as follows :

$$\boldsymbol{k}(t) = \frac{\gamma}{2\pi} \int_0^t G(\tau) d\tau \tag{1}$$

Hardware constraints on the maximum gradient amplitude (G_{max}) and slew rate (S_{max}) induce limitations in trajectory speed and acceleration. These limits can be expressed as inequality range constraints on each of the time points of the discrete waveform $\boldsymbol{k}[i]_{1 \leq i \leq p}$, where p is the number of gradient timesteps. For instance, the speed

constraint is expressed as follows:

$$\|\dot{\boldsymbol{k}}[i]\| = \left\| \frac{\boldsymbol{k}[i] - \boldsymbol{k}[i-1]}{dt} \right\| < \frac{\gamma}{2\pi} G_{max} \tag{2}$$

where dt is the gradient raster time. The acceleration constraint is expressed likewise. The raster time is fixed and typically equal to $dt = 10\,\mu s$ on the actual MR gradient coils. The k-space trajectory is sampled at a given sampling rate, also referred to as the readout bandwidth (rBW $= \frac{1}{\Delta t}$, where Δt is the interval between digitized samples also called *dwell time*).

Following our previous work [33, 15], our objective is to minimize a L^2 distance between a target density ρ and a sampling trajectory $\boldsymbol{k}$ under the aforementioned constraints :

$$\min_{\boldsymbol{k} \in Q_p} dist(\rho, v(\boldsymbol{k})) = \min_{\boldsymbol{k} \in Q_p} \frac{1}{2} \|h \star (v(\boldsymbol{k}) - \rho)\|_2^2 \tag{3}$$

where h is a continuous interpolation kernel, $v(\boldsymbol{k})$ is the discrete measure supported by the curve $\boldsymbol{k}$ (see [15, top of page 2052] for the definition of v) and Q_p is the set of curves respecting the aforementioned constraints. The symbol $\star$ denotes the convolution operator.

The distance in (Equation 3) can be conveniently rewritten by expanding the L^2-norm into:

$$\min_{\boldsymbol{k} \in Q_p} \underbrace{\frac{1}{p^2} \sum_{1 \le i,j \le p} H(\boldsymbol{k}[i] - \boldsymbol{k}[j])}_{F_r(\boldsymbol{k})} - \underbrace{\frac{1}{p} \sum_{i=1}^{p} \int_{\Omega} H(x - \boldsymbol{k}[i]) \rho(x)\, dx}_{F_a(\boldsymbol{k})} \tag{4}$$

where H is a well-chosen radial function. In our experiments, we selected the Euclidean distance $H(x) = -\|x\|_2$ [35, 15]. Problem (4) can be interpreted as the minimization of a potential energy $F(\boldsymbol{k}) = F_r(\boldsymbol{k}) - F_a(\boldsymbol{k})$ containing an attractive term F_a (bringing together samples according to the target density) and a repulsive term F_r (avoiding the formation of gaps and clusters of samples). After calculation of the derivatives of these two terms, this non-convex cost function can be minimized by a projected gradient descent of the type $\boldsymbol{k}_{t+1} = \Pi_{Q_p}(\boldsymbol{k}_t - \beta_t \nabla F(\boldsymbol{k}_t))$, which alternates between a non-convex distance minimization part and a projection onto the convex MR constraints Q_p. Let us note that the problem formulation in Equations (3) and (4) also accommodates to multiple segments when considering a shot-by-shot projection. Compared to the previous works [33], we accelerated the convergence by using a Barzilei-Borwein step-size rule [30], allowing to reducing the computing times by a factor ranging from 2 to 10. In addition, all segments of a SPARKLING trajectory are generated simultaneously using a multi-scale algorithm (i.e. doubling the number of particles p at each iteration) as shown in the Supporting Information Videos S1 and S2 (see Supporting Information for video legends).

Altogether, a non-Cartesian algorithm was implemented on Matlab (Release 2015b, the MathWorks Inc., Natick, MA, USA) to solve Problem (4). Typically, to generate the k-space trajectory in (Fig. 1a) (imaging matrix size: $N \times N$ with $N = 256$, 32 shots, 3072 gradient points per shot so $p = 98,304$ particles reached after 5 decimation levels), the computation time was about 10 minutes on a Intel dual Core i7-5600U CPU running at 2.60 GHz with 16GB RAM. Let us mention that as the resolution, readout duration and field-of-view change, new SPARKLING trajectories should be generated.

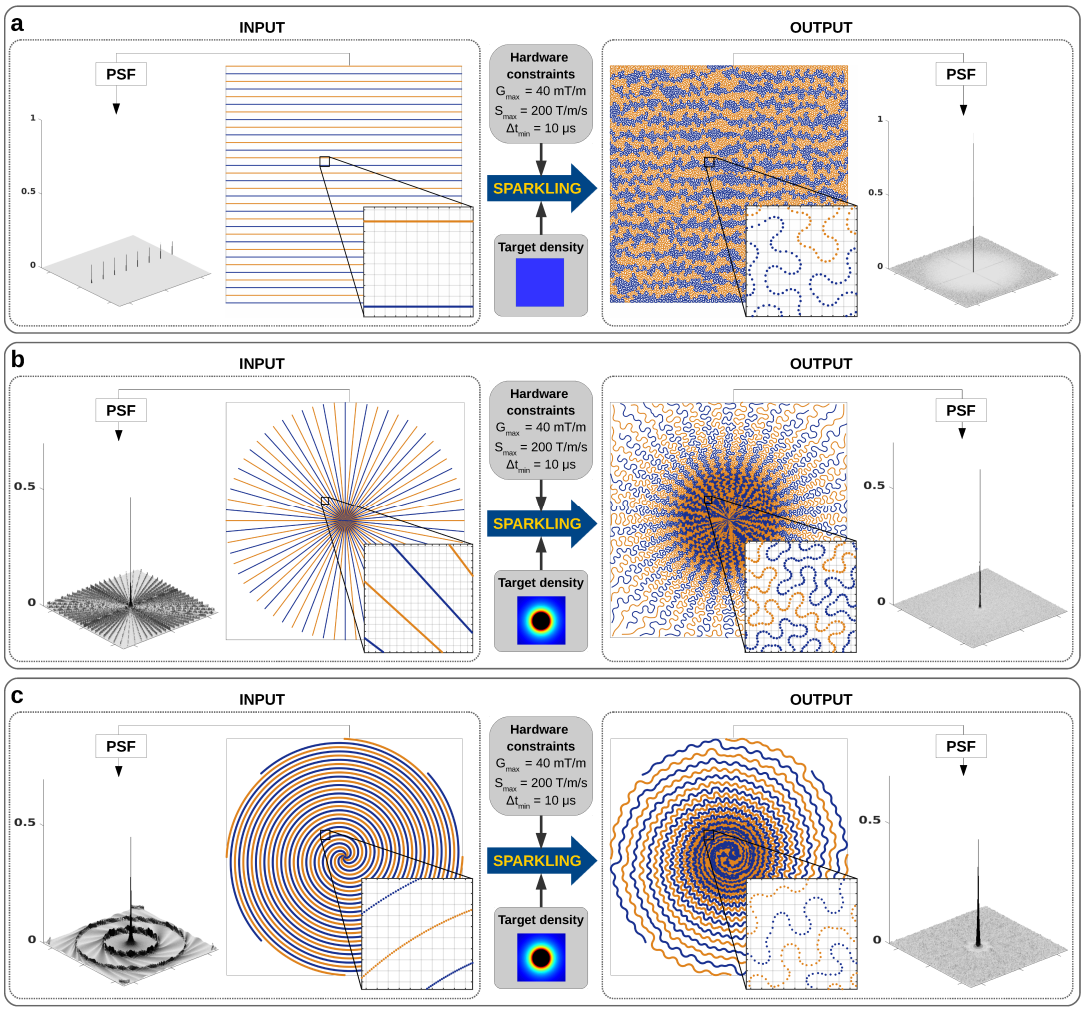

FIGURE 1 **Generation of SPARKLING trajectories for different initializations and target densities**. The maximum gradient amplitude and slew rate were $G_{max} = 40$ mT/m and $S_{max} = 200$ T/m/s, respectively. The duration of each segment was 30.72 ms, and the readout bandwidth was taken equal to the gradient bandwidth (rBW = $BW_{gradient} = 100$ kHz). **a**, The SPARKLING method applied to Cartesian lines with uniform density for $N = 256$ and 32 segments. **b**, The SPARKLING method applied to radial spokes with variable radial density for $N = 512$ and 34 symmetric segments. **c**, The SPARKLING method applied to centered-out Archimedean spiral initialization with variable radial density for $N = 256$ and 8 segments (not used in experiments).

| High receiver sampling rate

The selection of a proper bandwidth appeared to be critical to design efficient trajectories. In this paper, we suggest to use the highest possible bandwidth. The same idea guides spiral acquisitions, where a high sampling rate is used to rapidly sweep over a large portion of the k-space [36, 31]. There are three important reasons that motivate this choice.

First, although a higher readout bandwidth increases the amount of noise per sample, it also improves the temporal

resolution of the signal. This additional information is usually more valuable than the loss of signal. This is similar to the principle of Sigma-Delta quantization which can be shown to be advantageous from a theoretical point of view [37]. Second, it allows a better exploration of k-space by authorizing local circumvolutions as is illustrated in (Fig. 2). Third, the use of a high receiver bandwidth allows the filtering effects to be mitigated. These effects can actually lead to dramatic information losses for large dwell times [**?**]. Indeed, although k-space trajectories traverse a continuous path, the signal is sampled only at discrete intervals along the path. Because of the temporal bandlimiting filters of MR receiver hardware, the measured information is essentially averaged over pieces of trajectories comprised between two sampled points [38, 39, 40]. Hence, it was necessary to incorporate a third criterion in our trajectory design to minimize these filtering effects:

(iii) For each individual shot, assuming a certain sampling rate rBW, the distance between two consecutive samples should be smaller than the size of a k-space pixel $\Delta k = \frac{1}{\text{FOV}}$, where FOV is the field-of-view.

Criteria (iii) can easily be incorporated to the original algorithm by adjusting the speed limitation to:

$$\|\dot{\boldsymbol{k}}[i]\| < \min\left(\frac{\gamma}{2\pi} G_{max}, \frac{1}{\text{FOV} \cdot \Delta t}\right) \tag{5}$$

where Δt is the sampling interval. This additional requirement tends to straighten the trajectories, since they are designed so that consecutively acquired samples remain close to each other in the k-space. To relax this side effect, the readout sampling rate should therefore be chosen as large as possible (i.e. the dwelltime as small as possible).

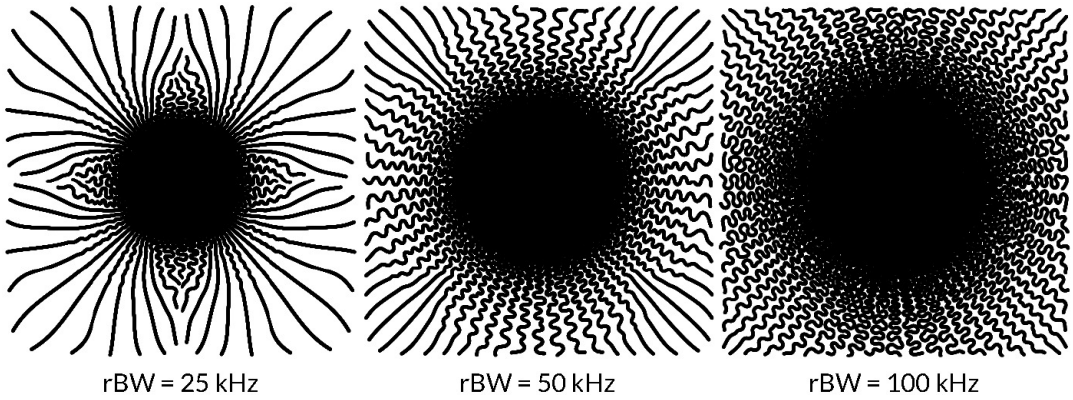

FIGURE 2 **Evolution of SPARKLING patterns as a function of the readout sampling rate**. Radial-initialized SPARKLING trajectories composed of 34 shots were generated for three growing readout sampling rates. From left to right, the readout bandwidth (rBW) is equal to 25 kHz, 50 kHz and 100 kHz respectively. Because the k-space path between two consecutive samples acquired along an individual shot is constrained to be smaller than the size of a k-space pixel ($\Delta k = 5\ m^{-1}$), the trajectories become more flexible and space-filling as the rBW increases. Excluding the readout sampling rate, all other parameters were kept constant and the same radially decaying target density was used. The readout duration was 30.72 ms, corresponding to 3072 gradient steps (displayed on the figures) per individual shot ($\text{BW}_{\text{gradient}} = 100$ kHz). The considered imaging matrix was 512×512, corresponding to a resolution of $390\ \mu\text{m} \times 390\ \mu\text{m}$.

In all our experiments, to avoid interpolation between the gradient timesteps, we acquired the ADC samples at a

rate of 100 kHz, which is equal to the gradient bandwidth: ADC samples and gradient samples are thus superimposed. Because MR data are sampled at a high rate and samples are optimally spread along a variable density adapted to compressed sensing, the proposed method allows to maximize the amount of information measured per shot for the given bandwidth, and thus to reduce the large number of shots needed for high resolution imaging. Hence, very high acceleration factor AF can be achieved while maintaining a relatively low subsampling factor R. R and AF are defined with respect to the fully sampled Cartesian acquisition (ground truth image), leading to the formulas $R = n/m$ and $AF = N/n_c$, where $n = N \times N$ is the number of pixels in the image, m is the number of collected ADC samples and n_c is the number of shots. The acceleration factor should thus be understood as a measure of sampling efficiency.

| Target density

The selection of a proper target density ρ is critical to obtain good reconstructions in the compressed sensing regime. This question is non trivial and currently subject to active research [41, 42, 14, 43, 44]. In particular, it should depend on the reconstruction algorithm and on the type of images probed. In this work, we focus on the case of radially symmetric densities, which present the advantage of yielding results invariant to translation and rotation of the sample to image. In addition, it will allow to perform comparisons with spiral trajectories which cannot cope with anisotropic densities contrarily to our approach. While radial densities are probably not the best possible choice for a given organ (e.g. a brain has many structures with a given orientation), it is a good candidate for universal sequences capable of probing arbitrary objects.

In the situation in which all segments of a k-space trajectory pass through the origin at a given echo time, the sample density at the origin is excessively high. Our objective was to provide a method to generate target densities that mitigate this effect. Considering n_c segments crossing the origin with a maximum speed α, the minimal density in the center of the k-space is that of the radial trajectories at the maximum speed (see Supporting Information Figure S3). The density of the radial curves at a constant speed is of type $f(k) = \frac{c}{|k|}$ for a certain c (at least asymptotically as n_c increases). However, this is only true within a given disk D_{r_0} of radius r_0 that we wish to determine. In practice, the distance between two circularly adjacent samples (denoted $\Delta_{rad}(j)$ for the j_{th} sample from the center) should be smaller than $\tau\Delta k_0$, where $\tau \in (0, 1]$ and $\Delta k_0 = \frac{1}{FOV}$ is the size of a k-space pixel. Nyquist's theorem suggests taking $\tau = 1$, but selecting a lower value ensures more stability, as it allows the use of smooth interpolation functions [37]. The condition on two circularly adjacent samples $\Delta_{rad}(\bar{j}) \leq \tau\Delta_{k_0}$ therefore gives $r_{\min} = \bar{j}\alpha\Delta t$, where Δt is the sampling interval and the index $\bar{j}$ is given by:

$$\bar{j} = \left\lceil \frac{\tau\Delta_{k_0}}{\alpha\Delta t_{min}\sqrt{2 - 2\cos(\pi/n_c)}} \right\rceil. \tag{6}$$

Furthermore, to determine the density inside the disk D_{r_0}, we use the fact that the total mass of the density inside the disk should be $\frac{n_c(\bar{j}+1)}{m}$, where m is the total number of samples. The value of constant c defining the density f should be such that:

$$\int_{B_0^{r_{\min}}} f(k)\, dk = \frac{n_c(\bar{j}+1)}{m}, \tag{7}$$

i.e.,

$$c = \frac{n_c(\bar{j}+1)}{m \int_{B_0^{r_{\min}}} \frac{1}{|k|}\, dk}. \tag{8}$$

Finally, we get:

$$f(k) = \frac{n_c(\bar{j}+1)}{m2\pi r_{\min}|k|}. \tag{9}$$

Given, an initial target density $\nu : k \mapsto \frac{1}{|k|^d}$, a value τ and the parameters describing the trajectory α, n_c and Δt, we generate an algorithm that returns a new target density ρ complying with the following three constraints:

1. Inside the disk $D_{r_0}, \rho = f$. Since the analytic expression of f was derived, it suffices to set $\rho(I) = f(I)$, where I is the set of indices with $|k| \leq r_{\min}$.
2. Two samples outside this disk should be separated by a distance greater than $\tau\Delta k_0$. The mean number of samples inside a pixel x of edge length Δ_{k_0} is $n_s\rho(x)$. If the samples are uniformly distributed in the pixel, the mean distance between adjacent pixels is $\frac{\Delta_{k_0}}{\sqrt{n_s\rho(x)}}$; we aimed for this distance to be greater than $\tau\Delta_{k_0}$. This means that ρ should satisfy:

$$\rho(x) \leq \frac{1}{n_s\tau^2} = \rho_{\max}. \tag{10}$$

3. ρ should be proportional to ν when possible. To satisfy this criterion, we designed an iterative algorithm as follows:
   - While $\max(\rho(I^c)) > \rho_{\max}$
     - Find $J = \{k \in I^c, \rho(k) > \rho_{\max}\}$.
     - Set $\rho(J) = \rho_{\max}$.
     - Normalize ρ in $I^c \setminus J$.

For simplicity, we assumed that ρ is constant on each pixel of edge size Δk_0.

| Output SPARKLING trajectories

We now show the output SPARKLING trajectories for different target densities and initializations. The considered hardware constraints were $G_{max} = 40$ mT/m and $S_{max} = 200$ T/m/s for the gradient and the slew rate respectively.

| Uniform sampling

To illustrate the versatility of the proposed approach, we first consider a uniform density without undersampling for an acceleration factor of $AF = 8$ and an imaging matrix of 256×256. Classically, the fully sampled Cartesian acquisition would measure 512 samples (oversampling factor of 2) along 256 Cartesian lines to fill the k-space grid. (Fig. 1a) displays how our process transforms an initial Cartesian trajectory composed of 32 parallel lines, which corresponds to $AF = 8$. Here, the considered readout duration is 30.72 ms, corresponding to 3072 samples (rBW = $\text{BW}_{\text{gradient}} = 100$ kHz), with the idea to perform T_2^*-weighted acquisitions [45]. Our optimization algorithm deforms these straight lines and uniformly scatters the non-Cartesian samples along highly sinuous curves. In this case, despite high acceleration ($AF = 8$), the acquisition is not subsampled ($R = 0.66$). (Supporting Information Video S1) shows the generation of the SPARKLING sampling in (Fig. 1a) and illustrates how samples are spread to maximize coverage.

| Variable-density sampling

The proposed method is particularly relevant in the context of compressed sensing where large acceleration factors can be attained. The results of such variable-density k-space trajectories are presented for a radial initialization in (Fig. 1b) and for an Archimedean spiral initialization in (Fig. 1c). In both cases, the input initializations did not originally comply with the gradient hardware constraints, the target density was radially decreasing, and the considered readout duration was also 30.72 ms. (Supporting Information Video S2) shows the dynamic generation of the SPARKLING sampling in (Fig. 1b). (Fig. 1a-c) also displays the point spread functions (PSFs) of both the input and output k-space trajectories, defined as the modulus of the Fourier transform of the sampling pattern viewed as a set of Dirac impulses. This result shows how the proposed method improves the PSF properties by transforming coherent patterns that are sources of artifacts into incoherent noise, which is easily removed with nonlinear reconstructions. The output central peak is also better defined than initially and is surrounded by a low-energy annulus, yielding higher image quality [46, 47]. In addition, (Fig. 3a) displays the SPARKLING trajectory composed of 16 spokes of 3072 samples used to produce the brain image in Fig. (6b), corresponding to a 16-fold acceleration for an image size of 256×256.

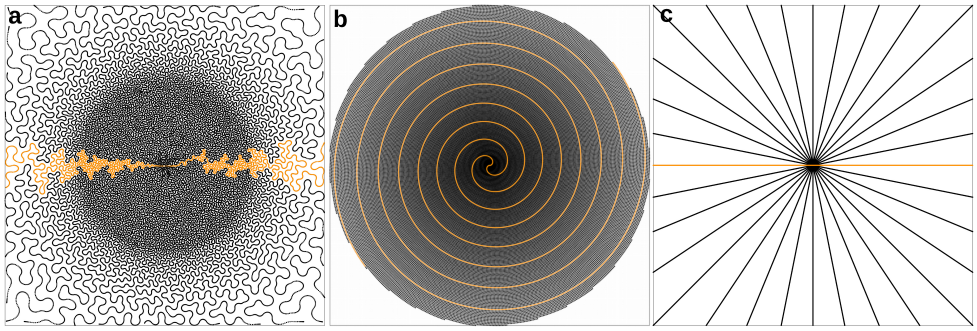

FIGURE 3 The SPARKLING (**a**), variable-density spiral (**b**) and radial (**c**) trajectories used for *ex vivo* comparisons. The considered imaging matrix was 256×256, corresponding to a resolution of $780\ \mu m \times 780\ \mu m$. Each trajectory is composed of 16 symmetric segments of 3072 samples (an individual shot is highlighted in yellow), resulting in an acceleration factor of $AF = 16$ and a subsampling factor of $R = 1.33$.

In (Fig. 4), we display the typical gradient and slew rate waveforms of a 26-shot radially initialized SPARKLING trajectory lasting 30.72 ms. While the slew rate is saturated, the maximum allowed gradient amplitude is not reached in this case. Here, criterion (iii) limits the speed of the SPARKLING trajectory to about 12 mT/m.

| METHODS

The first set of experiments involved an *ex vivo* human brain, which allowed assessing the performance of the proposed strategy independently from motion and physiological considerations. The human brain used for this study was obtained via the body donation program of University of Tours, France from a donor who gave his written consent before death. The brain was extracted and fixed in formalin (formaldehyde solution at 37 % m/m, Cooper, Melun, France) diluted in tap water to obtain a formalin concentration of 10 %). The *ex vivo* phantom was then immersed in a proton-free perfluorinated liquid before the acquisitions.

Second, acquisitions were also performed *in vivo* on four healthy volunteers to validate the clinical potential of the

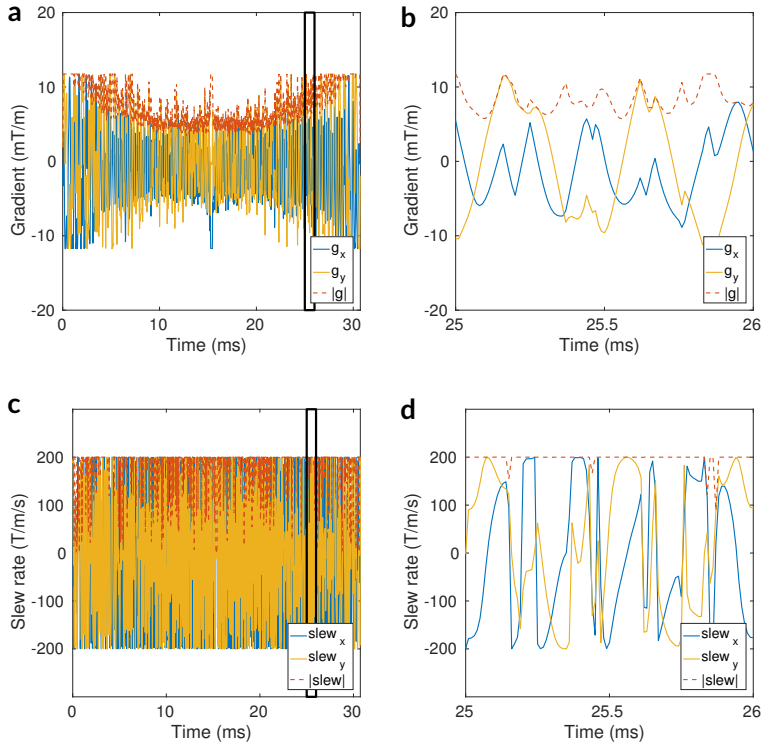

FIGURE 4 **Gradient and slew rate waveforms of a 26-shot radially initialized SPARKLING trajectory**. In (**a**), the gradients on the x- and y- directions are respectively displayed in blue and yellow for the first shot. The corresponding vector magnitude is in orange dashed lines. (**b**) shows the magnified region outlined in the black box in (**a**). The maximum allowed gradient amplitude on the scanner was 40 mT/m. In (**c**), the slew rates on the x- and y- directions are respectively displayed in blue and yellow. The corresponding vector magnitude is in orange dashed lines. (**d**) shows the magnified region outlined in the black box in (**c**). The maximum allowed slew rate was 200 T/m/s.

approach. The *in vivo* human experiments were approved by a national ethics committee (CPP IDF 7 Kremlin-Bicêtre) under the protocol registration number 07-042. All volunteers signed a written informed consent form.

Following typical high-field sequence specifications [45], we considered a T_2^* contrast with an echo time of 30 ms and a readout of 30.72 ms for both *in vivo* and *ex vivo* experiments. The long repetition time (550 ms) allows to acquire 11 interleaved slices per excitation, but in what follows, reconstructions are only displayed for one slice. In all the experiments, we used radially initialized in-out SPARKLING trajectories. To assess the performance of our method, we compared it with the two most widespread non-Cartesian trajectories in MRI: radial and variable-density spiral trajectories. The collected multi-channel non-Cartesian data were reconstructed using a ℓ^1-based nonlinear reconstruction algorithm suggested in compressed sensing, which does not account for distortions [48, 49].

| Design of spiral trajectories

Variable-density spiral trajectories were designed using a variable effective FOV as described in [50], with a maximum slew rate of $S_{max} = 200$ T/m/s. A symmetric segment was obtained by joining two opposing center-out spiral inter-

leaves [51] in order for the echo time to be half of the readout time. The total duration of one interleaf was set to 30.72 ms by tuning the parameters controlling the linear variable-density trajectory and the peak gradient amplitude was between 20 and 30 mT/m. (Fig. 3b) displays the variable-density spiral sampling composed of 16 interleaves of 3072 samples used to produce the brain image in (Fig. 6c), corresponding to a 16-fold acceleration for an image size of 256×256.

| Design of radial trajectories

Radial trajectories were designed using a trapezoid gradient waveform, with a ramp time of 0.1 ms until reaching a plateau amplitude of 0.98 mT/m and 1.96 mT/m for images sizes of 256×256 and 512×512, respectively, such that the readout time was 30.72 ms. Radial spokes crossed the origin of the k-space at their middle time point and were designed to reach the corners of the k-space. (Fig. 3c) displays the radial sampling composed of 16 spokes of 3072 samples each, which were used to produce the brain image in (Fig. 6d), corresponding to a 16-fold acceleration for an image size of 256×256.

| Acquisitions

All acquisitions were performed on a 7 Tesla MR scanner (Siemens Healthineers, Erlangen, Germany) with a 1Tx/32Rx head coil (Nova Medical, Wilmington, MA, USA) and a head-only gradient system (AC84). The maximum gradient amplitude and slew rate for this system were 50 mT/m and 333 T/m/s, respectively. For the T_2^*-weighted acquisitions, a 2D GRE sequence was modified to allow execution of arbitrary gradient waveforms complying with the hardware constraints. All non-Cartesian trajectories were acquired using this sequence and the same parameters. The repetition time, echo time and observation time were 550 ms, 30 ms and 30.72 ms, respectively. The FOV was 20 cm, and the flip angle was 25 degrees. Two resolutions were investigated: $390\ \mu\text{m} \times 390\ \mu\text{m} \times 3$ mm and $780\ \mu\text{m} \times 780\ \mu\text{m} \times 1.5$ mm, corresponding to matrix sizes of 512×512 and 256×256, respectively. Standard shimming was performed on the studied slice for *ex vivo* acquisitions and on the whole brain volume for *in vivo* experiments. The sampling bandwidth was equal to the gradient bandwidth: $\text{rBW} = \text{BW}_{\text{gradient}} = 100$ kHz.

For the 8-fold accelerated Cartesian acquisition using online GRAPPA reconstruction (Fig. 5d-h), the same GRE sequence was used with Integrated Parallel Acceleration Technology. This sequence acquires 24 reference lines for auto-calibration. Sequence parameters were the same as above and the default oversampling factor of 2 was used for a base resolution of 256.

| Self-calibrating nonlinear reconstruction

2D MR image reconstructions were performed by iteratively minimizing a sparsity promoting regularized Compressed Sensing SENsitivity Encoding (CS-SENSE) criterion introduced in [52, 53, 54]. We adopted a synthesis formulation composed of an ℓ_2-norm data consistency term and an ℓ_1-norm penalty term, which reads as follows:

$$\widehat{\mathbf{z}} = \underset{\mathbf{z} \in \mathbb{C}^{N \times N}}{\arg\min} \frac{1}{2} \sum_{\ell=1}^{L} \|F_\Omega \mathbf{S}_\ell \boldsymbol{\Psi} \mathbf{z} - \mathbf{y}_\ell\|_2^2 + \lambda \|\mathbf{z}\|_1 . \tag{11}$$

The decomposition ($\widehat{\mathbf{z}}$) is then transformed back to the image domain by using the synthesis operator $\boldsymbol{\Psi}$: $\widehat{\mathbf{x}} = \boldsymbol{\Psi}\widehat{\mathbf{z}}$. In our experiments, $\boldsymbol{\Psi}$ was chosen as an orthogonal wavelet transform using the Symmlet of order 8 as the mother wavelet

basis function. We used $J = 4$ levels of decompositions, i.e., 12 sub-bands of detail coefficients for encoding horizontal, vertical and diagonal details on top of the low-frequency approximation. The sum of squares term in (11) encodes parallel reception over the $L = 32$ channels of our phased array coil. $\mathbf{y}_l \in \mathbb{C}^m$ represents the measured Fourier values of the ℓ^{th} coil. To handle non-Cartesian Fourier samples, the non-equispaced fast Fourier transform (NFFT, version 3.2.3) [55] was therefore used to compute F_Ω. The NFFT takes non-uniformly sampled k-space measurements as input data and returns an image on the Cartesian grid. The matrix $\mathbf{S}_\ell \in \mathbb{C}^{n\times n}$ ($n = N \times N$) in (11) is diagonal and represents the sensitivity map associated with the ℓ^{th} coil that enhances the specific spatial domain of the desired image $\widehat{\mathbf{x}}$. To estimate the sensitivity maps $\{\mathbf{S}_\ell\}_{\ell=1:L}$, we extended a self-calibrated method used in SAKE [56] or IRGN [57] to the non-Cartesian setting, as explained below. First, for each coil, a low-resolution $N \times N$ image was reconstructed using the central surface representing 20 % of the collected k-space completed by zero-filling: $\mathbf{x}_\ell^{\text{LR}} = F^{\star}_{[\Omega_{|20\%},\mathbf{0}]}\mathbf{y}_\ell$, where LR stands for low resolution and F^* defines the adjoint operator of the NFFT. Second, the square root of the sum of squares (SSOS) was computed: $\mathbf{w} = \sqrt{\sum_{\ell=1}^{L} \|\mathbf{x}_\ell^{\text{LR}}\|^2}$. Third, the sensitivity maps were given by the pixelwise ratio of the low-resolution image coils and the SSOS: $[s_\ell]_i = \text{diag}[\mathbf{S}_\ell]_{ii} = \left[\mathbf{x}_\ell^{\text{LR}}\right]_i / \mathbf{w}_i$, $\forall \ell = 1:L, (i = 1:n)$. Because of this SSOS operation, our method is less dependent on the threshold (i.e., 20 %) over the central surface of the k-space than the method of [58], who directly exploits the $\mathbf{x}_\ell^{\text{LR}}$ images as sensitivity map information. Once the sensitivity maps were estimated, an accelerated proximal gradient method [59] was implemented to solve (11). The regularization parameter λ controls the trade-off between data consistency and confidence in the sparsity prior, and this parameter was tuned manually over a discrete grid of values within the interval $[10^{-7}; 10^{-4}]$. In practice, we conducted image reconstructions for each value over this grid and retained the setting with the highest visual quality. The reconstruction times were approximately 4 and 8 minutes for matrix sizes of $n = 256 \times 256$ and $n = 512 \times 512$ respectively. In all the text, the acquired, reconstructed and displayed pixel dimensions are equal.

| RESULTS

| *Ex vivo* results

Prospective results of the SPARKLING strategy initialized with Cartesian lines for a T_2^*-weighted contrast are displayed in (Fig. 5) in the case of the uniform-density output shown in (Fig. 1a). The acquisition performed with the SPARKLING trajectories thus lasted 16 s, which is 8 times shorter than the fully sampled Cartesian acquisition with an acquisition duration of 2 min 20 s for 11 slices. SPARKLING images reconstructed with nonlinear compressed sensing reconstructions are displayed in (Fig. 5b-f). We also show in (Fig. 5c-g) the results of a simple gridding method to reconstruct the SPARKLING data. Both reconstructions show very little difference from the fully sampled Cartesian reference (Fig. 5a-e), although the gridding reconstruction may be slightly noisier (Fig. 5g) than the nonlinear reconstruction (Fig. 5f). The data corresponding to the input trajectory of 32 Cartesian lines (oversampled by a factor of 2) in (Fig. 1a) can be typically processed online with a GRAPPA reconstruction [10] available on the MR scanner to produce the image in (Fig. 5d-h). The degradation of the image quality, along with a significant decrease in the SNR, is clearly observed (Fig. 5h). Although GRAPPA acceleration factors rarely exceed 4 in 2D Cartesian scans, we wanted to push the limits of this product sequence to match our acceleration.

The radially initialized SPARKLING strategy similar to that in (Fig. 1b) was also compared to widely used radial and variable-density spiral trajectories for an in-plane resolution of 780 μm and a slice thickness of 1.5 mm (Fig. 6). All three acquisitions lasted 8.8 s and involved 16 segments, corresponding to a 16-fold acceleration relative to the fully sampled Cartesian reference with an acquisition duration of 2 min 20 s for 11 slices. The subsampling factor was in that case $R = 1.33$, as the long readout duration of 30.72 ms allowed the measurement of many samples per shot (3072

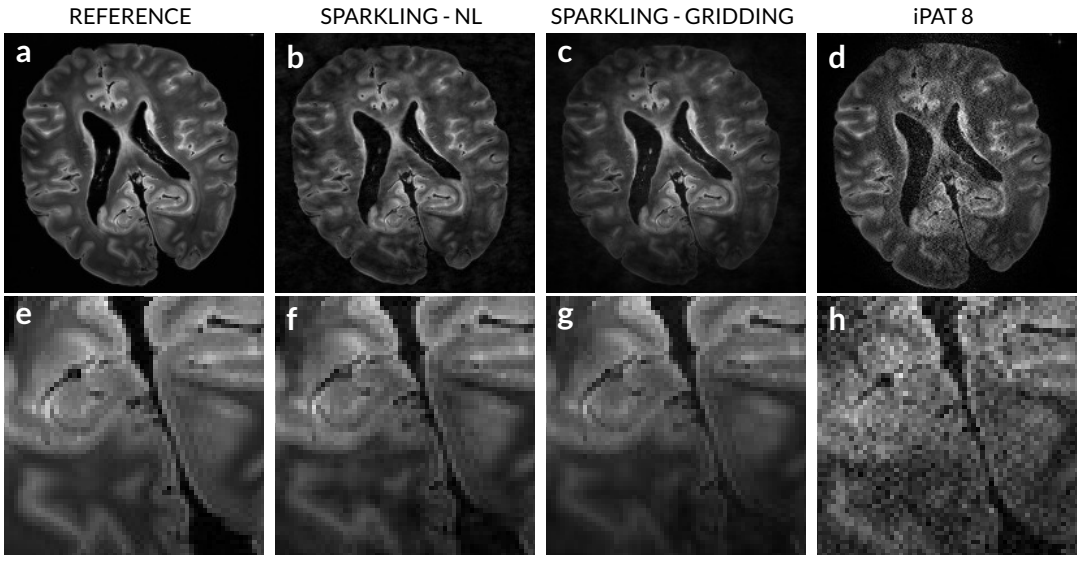

FIGURE 5 **Prospective validation of SPARKLING trajectories.** Acquisitions performed on a *ex vivo* human brain for uniform-density SPARKLING sampling (Fig. 1a output) at a resolution of 780 μm $\times$ 780 μm $\times$ 1.5 mm and a total of 32 shots ($AF = 8$ and $R = 0.66$). **a**, A fully sampled Cartesian reference lasting 2 min 20 s for 11 slices. **b**,**f**, Image reconstructed using nonlinear methods from SPARKLING acquisition lasting 16 s. **c**, Image reconstructed from the same SPARKLING acquisition using a gridding method. **d**, Image acquired with the input Cartesian trajectory of (Fig. 1a) and reconstructed with a GRAPPA method available on a Siemens scanner (integrated parallel acceleration technology with a factor of 8), whose acquisition time was 16 s. **e**,**f**,**g**,**h**, Magnified region of interest in the medial part of the parieto-occipital cortex (delimited by a yellow square in **a**) of images **a**,**b**,**c**, and **d**, respectively. Image reconstructions did not include any correction of system imperfections.

samples per shot). Using the same nonlinear reconstruction pipeline, the resulting images (top row) and corresponding magnified images of a region of interest in the medial parieto-occipital cortex (bottom row) are shown in (Fig. 6b-f) for the SPARKLING trajectory, (Fig. 6c-g) for the variable-density spiral trajectory and (Fig. 6d-h) for the radial trajectory. First, let us highlight the presence of dark areas at the top of the image in the Cartesian images (probably due to off-resonance effects). The SPARKLING reconstruction remains similar to the fully sampled Cartesian reference (Fig. 6a-e) despite a slight loss of resolution visible on the smallest details of the brain. In comparison, the high acceleration factor severely impairs the results of the variable-density spiral and radial reconstructions. The accelerated radial trajectory generates a blurry image, illustrating the inefficiency of oversampling radial spokes. The more efficient variable-density spiral trajectory produces a higher-quality image; however the image contains notable off-resonance artifacts along the cortical surface of the brain (Fig. 6c) as well as in finer structures visible in the magnified image (Fig. 6g).

Acquisitions were also performed with a higher in-plane resolution of 390 μm and three acceleration factors $AF = 10, 15, 20$. The SPARKLING trajectories were initialized with radial patterns; the 15-fold accelerated SPARKLING trajectory corresponds to the output of (Fig. 1b). The resulting SPARKLING images and corresponding magnified images are displayed in (Fig. 7c-d) for $AF = 10$ (51 shots), (Fig. 7e) for $AF = 15$ (34 shots) and (Fig. 7f) for $AF = 20$ (26 shots). When focusing on fine brain structures in the medial parieto-occipital cortex, the stability of image quality using SPARKLING trajectories with increasing acceleration factors is observed. In addition, the images produced with the SPARKLING sequence, despite their very short acquisition times, e.g. 14 s for 11 slices for the highest acceleration

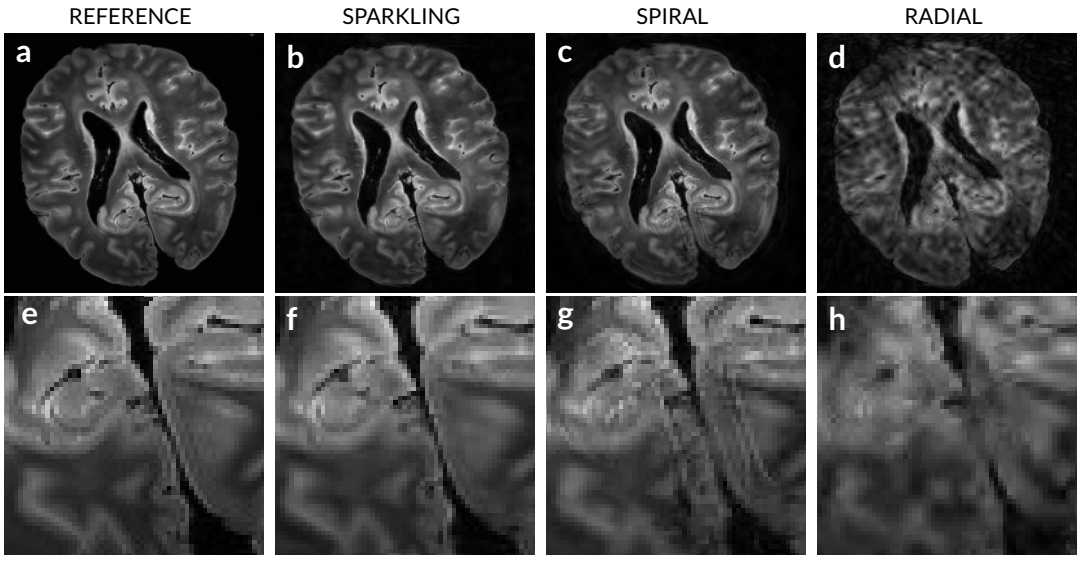

FIGURE 6 **Comparison of SPARKLING sampling with variable-density spiral and radial trajectories**. *Ex vivo* acquisition presenting a resolution of 780 μm $\times$ 780 μm $\times$ 1.5 mm and a total of 16 shots ($AF = 16$ and $R = 1.33$). **a**, T_2^*-weighted reference image and a magnified region of interest in the parieto-occipital cortex in **e** acquired with a fully sampled Cartesian acquisition lasting 2 min 20 s for 11 slices. **b**,**f**, Image reconstructed from a 16-fold-accelerated SPARKLING-generated acquisition lasting 8.8 s. **c**,**g**, Image reconstructed from a 16-fold-accelerated variable-density spiral acquisition lasting 8.8 s. **d**,**h**, Image reconstructed from a 16-fold accelerated radial acquisition lasting 8.8 s. Image reconstructions did not include any correction of system imperfections.

factor (Fig. 7f), maintain high similarity to the fully sampled Cartesian reference, which was obtained with an acquisition time of 4 min 42 s (Fig. 7a-b). Likewise, variable-density spiral and radial acquisitions with increasing acceleration factors are displayed in (Fig. 7g-j) and (Fig. 7k-n), respectively. In contrast to the SPARKLING reconstructions, the spiral acquisition yielded substantially more artifacts and the undersampled radial patterns produced an overly smoothed image presenting streaking artifacts at $AF = 20$. Let us mention that the signal bandwidth for the fastest spiral scans (26 shots) was lower than that theoretically required in the high frequencies (100 kHz instead of 400 kHz). Based on an image acquired with the correct signal bandwidth, we believe that this is unlikely to have caused significant artifacts. Moreover, we noted a slight diffeomorphism between the reference image and the images acquired with the non-Cartesian trajectories, certainly due to off-resonance effects induced by residual air bubbles in the phantom. This is why we did not perform quantitative measures of the image quality.

| *In vivo* results

T_2^*-weighted acquisitions were also performed *in vivo* on four healthy volunteers at an image resolution of 390 μm $\times$ 390 μm $\times$ 3 mm.

(Fig. 8) shows the brain images of two different subjects for an axial orientation in (Fig. 8**a**-**c**) and (Fig. 8**d**-**f**) and of a third subject for a coronal orientation in (Fig. 8**g**). The axial reference scan in (Fig. 8**a**,**d**) lasted 4 min 42 s for 11 slices while the acquisition times of the 8-fold and 15-fold accelerated SPARKLING scan were 35 s and 18 s respectively. The high target image quality was fairly well maintained even for the 34-shot SPARKLING trajectory (AF=16). Typically,

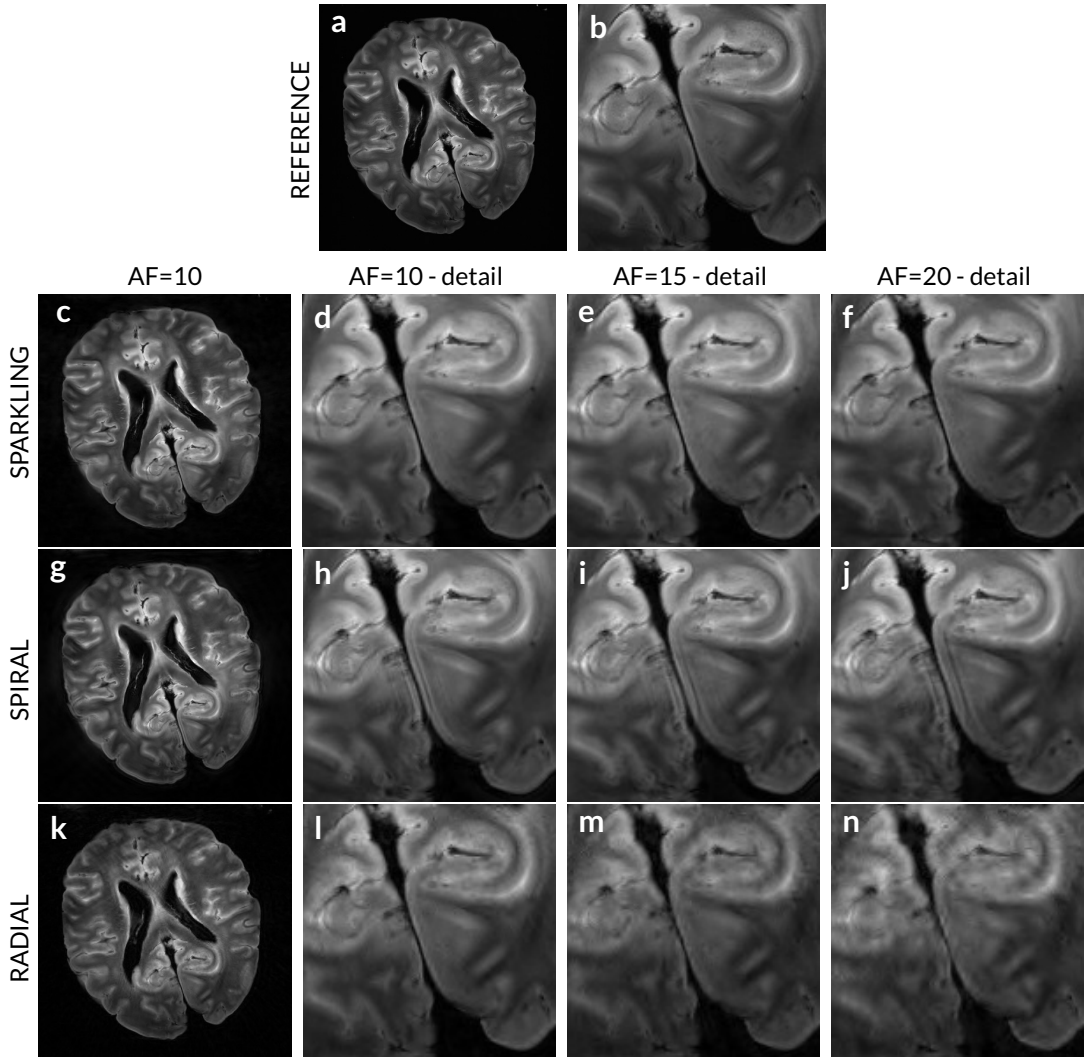

FIGURE 7 **Robustness of radial-initialized SPARKLING to very high acceleration factors**. Acquisitions performed on an *ex vivo* human brain for an image resolution of 390 μm $\times$ 390 μm $\times$ 3 mm and with acceleration factors ranging from $AF = 10$ to $AF = 20$. **a**,**b**, T_2^*-weighted reference image acquired with a fully sampled Cartesian acquisition lasting 4 min 42 s for 11 slices and a magnified region of interest in the parieto-occipital junction. Image reconstructed from 51 shots (28 s) and magnified region of interest are respectively displayed in **c**,**d** for SPARKLING sampling, **g**,**h** for variable-density spiral sampling and **k**,**l** for radial sampling. Magnified images reconstructed from 34 shots (18 s) are displayed in **e** for SPARKLING sampling, **i** for spiral sampling and **m** for radial sampling. Magnified images reconstructed from 26 shots (14 s) are displayed in **f** for SPARKLING sampling, **j** for spiral sampling and **n** for radial sampling. Image reconstructions did not include any correction of system imperfections.

the majority of vessels can be distinguished in the accelerated SPARKLING images although the smallest vessels were slightly blurred in the 15-fold acceleration. (Fig. 8**g**) displays a set of multiple coronal slices acquired with a SPARKLING

trajectory composed of 51 shots, lasting 28 s (AF=10). Consistent contrast and level of detail were obtained in all 11 slices.

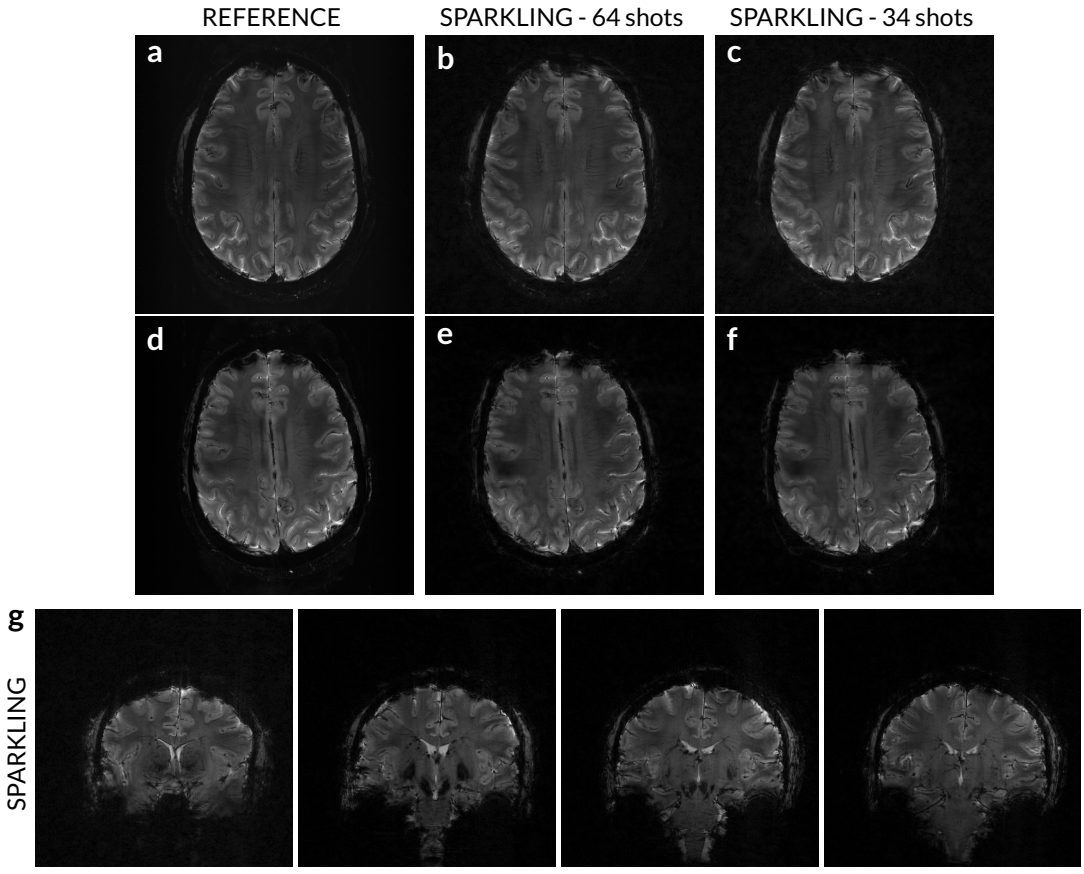

FIGURE 8 ***In vivo*** **SPARKLING results on 3 different subjects at an image resolution of 390** μ**m** $\times$ **390** μ**m** $\times$ **3 mm.** Axial acquisitions were performed on two different subjects (**a**-**c**) and (**d**-**f**) respectively. The fully-sampled reference scan is displayed on the first column (**a** and **d**), while the SPARKLING acquisitions composed of 64 (AF=8) and 34 (AF=15) shots are respectively shown on the second (**b**-**e**) and third (**c**-**f**) columns. The acquisition time for 11 slices was 4 min 42 s for the reference, 35 s for the 64-shot SPARKLING acquisition and 18 s for the 34-shot SPARKLING acquisition. The bottom row (**g**) displays multiple coronal slices of a third subject, acquired with a 51-shot (AF=10) SPARKLING trajectory (TA=28 s). Image reconstructions did not include any correction of system imperfections.

Furthermore, consistent with the *ex vivo* results, the *in vivo* results showed that the proposed SPARKLING strategy outperformed the conventional variable-density spiral and radial trajectories in all cases. The results from one subject are presented in (Fig. 9) for the highest studied acceleration factor, $AF = 20$, corresponding to 26 shots. Notice that all images suffer from off-resonance effects resulting in darker regions on the top of the image. (Fig. 9b) shows the image reconstructed from the SPARKLING acquisition lasting 14 s for 11 slices. Compared to the reference (Fig. 9a), which was obtained in an acquisition time of 4 min 42 s, the SPARKLING result was able to maintain the image quality fairly well despite a slight loss of resolution visible on the smallest vessels. However, the spiral acquisition at the same

acceleration factor (Fig. 9c,g) has notably more artifacts, and the 20-fold-accelerated radial reconstruction (Fig. 9d,h) appears blurry and presents streaking artifacts.

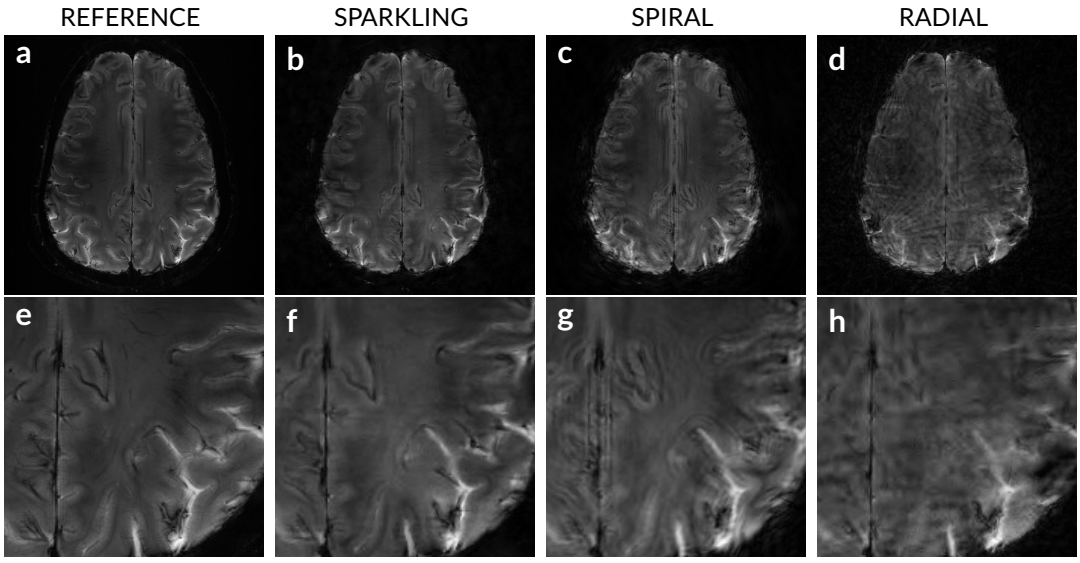

FIGURE 9 ***In vivo*** **validation of radial-initialized SPARKLING trajectories composed of 26 shots (AF=20) and comparison with spiral and radial sampling**. T_2^*-weighted GRE acquisition on a 7 Tesla scanner at an image resolution of 390 μm $\times$ 390 μm $\times$ 3 mm. **a**,**e**, Fully sampled Cartesian reference with an acquisition time of 4 min 42 s for 11 slices and a magnified region of interest in the parieto-occipital cortex. **b**,**f**, Image and magnified image reconstructed from a 20-fold-accelerated variable-density SPARKLING acquisition lasting 14 s for 11 slices. **c**,**g**, Image and magnified image reconstructed from a 20-fold accelerated variable-density spiral acquisition lasting 14 s. **d**,**h**, Image and magnified image reconstructed from a 20-fold accelerated radial acquisition lasting 14 s. Image reconstructions did not include any correction of system imperfections.

| Sensitivity to imaging imperfections

To evaluate the SPARKLING trajectories' sensitivity to imaging imperfections, we performed two simulations. One seeks to assess the sensitivity to gradient system imperfections and the other to off-resonance effects. We compared the SPARKLING and spiral trajectories.

| Gradient imperfections

Sensitivity to gradient imperfections can be simulated by considering a simple linear and time-invariant model of the gradient system. Under this assumption, the gradient system's behavior is fully described by its impulse response functions, which are called the gradient impulse response functions (GIRF) [60]. Given the general low-pass characteristics of gradient coils and amplifiers, the self-term GIRFs can be approximated by low-pass filters. To produce (Fig. 10), low-pass filtering was performed on a spiral and a SPARKLING shots. After bilateral zero-padding of corresponding

gradient waveforms in the time domain, a symmetric low-pass rectangular kernel of width 20 was applied to the input gradients by multiplication in the Fourier domain as described in [8]. After inverse discrete Fourier transform, the output trajectories were obtained by time integration. (Fig. 10) shows the effects of low-pass filtering on one shot of the spiral (in blue) and the radial-initialized SPARKLING (in orange) trajectories used for the 20-fold accelerated *in vivo* experiments in (Fig. 9). The simulated errors are represented as arrows departing from the nominal trajectories in a magnified region of the k-space center. The error vectors tend to point in the direction of the inward-pointing normal. Compared to the spiral errors, the SPARKLING ones are not only smaller in magnitude but also present random directions. This simple experiment provides an insight on why the SPARKLING patterns may be less sensitive to gradient errors than spiral patterns, even though a full validation would require measuring the trajectories either using gradient measurement method such as [4] or a dynamic field camera such as [61]. Further comparisons should also be performed in conjunction with a correction of gradient imperfections [8], since the SPARKLING trajectories may be harder to correct.

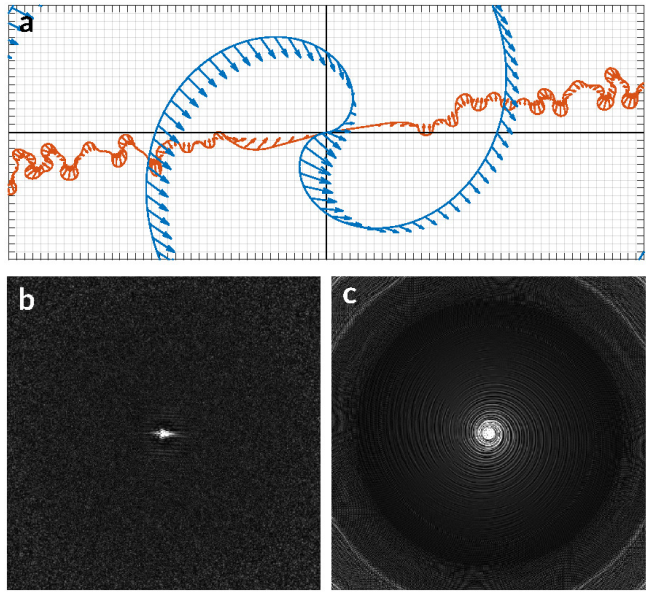

FIGURE 10 **Simulating the effects of system imperfections on SPARKLING and spiral trajectories**. (Top row): To simulate trajectory errors, the gradients corresponding to an individual segment of a spiral trajectory (in blue) and a sparkling trajectory (in orange) were filtered with the same low-pass filter. A magnified region of the center of the k-space shows the nominal trajectories and the corresponding error vectors represented as arrows. Compared to the simulated trajectory errors of the spiral, the ones of SPARKLING are of smaller magnitude and present random directions. The gridded background corresponds to the Cartesian grid for the considered FOV. (Bottom row): Simulated off-resonance PSF of radially initialized SPARKLING and spiral in-out trajectories. The off-resonance PSF of 34-shot SPARKLING (**b**) and spiral (**c**) trajectories were simulated for a frequency offset of 25 Hz. The readout duration was 30.72 ms for both trajectories. The main lobe of the spiral PSF is visibly wider than the one of the SPARKLING PSF. PSFs were normalized so as to ensure the integral of the magnitude square of the PSF over all space be 1. Color axis scaling is between 0 and 0.01.

| Off-resonance effects

We also simulated the off-resonance effects on the SPARKLING trajectories and compared them to spiral patterns. The PSF corresponding to a frequency offset of 25 Hz was computed for both sampling patterns and the results are displayed in (Fig. 10b-c). The main lobe of the spiral off-resonance PSF is visibly wider than the SPARKLING one. Structured spiraled patterns are also apparent in the spiral PSF while the SPARKLING PSF presents an incoherent structure. Moreover, a directional deformation (horizontal) can be observed on the SPARKLING off-resonance PSF. This may be due to the radial characteristics of the SPARKLING trajectory. Nevertheless, the off-resonance effects on SPARKLING will require further study. In particular, a better understanding of the anisotropic broadening of the main lobe and the effects of the diffuse side lobes would be informative.

| DISCUSSION

Since the invention of MRI, simple geometrical curves have dominated the landscape of sampling trajectories. In this work, we demonstrated that gradient performance allows the successful use of more complex and efficient variable-density sampling patterns which are near-optimal for compressed sensing [62]. Using the non-Cartesian SPARKLING framework, it is hence possible to generate optimized sampling trajectories fulfilling the aforementioned key criteria of truly controlled sampling density, locally uniform coverage and controlled k-space path between consecutive samples. Given any MR protocol characterized by its echo time (TE) and readout duration (Tobs), the presented optimization-driven method should thus be able to enhance MR sampling performance and reduce the number of shots in segmented acquisitions.

In this study, prospective accelerated acquisitions using SPARKLING trajectories were performed on a 7 Tesla scanner for a T_2^* contrast. The quality of these images was well maintained at high in-plane resolutions of 390 μm and 780 μm both *ex vivo* and *in vivo*, although our reconstructions did not involve any correction for imaging imperfections. The reproducibility of the approach was tested *in vivo* on four different subjects for both axial and coronal orientations. Moreover, the stability of this method was established even for very high acceleration factors of up to AF=20 (26 shots), at which the image quality was fairly preserved except for some of the smallest vessels that appeared blurry. However, we wish to emphasize that the evaluation of image quality is based on a non-blinded qualitative assessment by the authors and a more thorough comparison should be performed by clinicians. The versatility of the SPARKLING approach in terms of initialization and density inputs was corroborated in practice with the implementation of both uniform and variable-density sampling initialized either with Cartesian lines or radial spokes. The quality of the SPARKLING trajectory depends on the initialization of the algorithm. For instance, a spiral initialization is expected to be more sensitive to imaging imperfections (e.g., inter-shot inconsistency, off-resonance effects etc.) compared to a radial initialization. This hypothesis is supported by simulated experiments shown in the Supporting Information Figure S4.

Furthermore, our sampling strategy was shown to be 5 to 7 times faster than the standard acceleration techniques available on the scanner (iPAT) to achieve acceptable image quality for T_2^*-weighting. Compared to 2D radial trajectories, the optimized variable-density SPARKLING sampling also yielded perceptually higher image quality. Although the comparison with radial sampling has some limitations insofar as this strategy is usually more efficiently used with shorter readouts (like Cartesian sampling), this result highlights the benefits of our optimized trajectories compared to their radial initialization which was given as input of the algorithm. Furthermore, compared to variable-density in-out spiral which is adapted to long readout scenarios, the optimized variable-density SPARKLING sampling also presented a perceptually higher image quality deprived of artifacts. Let us mention that EPI-based trajectories were not considered in this work which focuses on variable-density sampling patterns. The similar results of *ex vivo* and *in*

vivo experiments prove that motion was not a discriminating element in these cases. Despite the long readout duration for the T_2^*-weighted acquisition (30.72 ms), our method was relatively less sensitive to system imperfections such as magnetic field inhomogeneity or trajectory errors, while spiral acquisitions presented important artifacts, as often reported in the literature [63, 64, 65, 31]. A comparison of the simulated off-resonance PSFs suggests that SPARKLING trajectories are more robust to off-resonance effects compared to spiral patterns for which the main lobe of the PSF was more widened. However, these preliminary simulations should be validated by further experiments. In spite of its sinuous appearance, SPARKLING patterns did not seem to suffer much from trajectory distortions which usually lead to severe image artifacts especially in non-Cartesian scanning due to inter-shot inconsistency in spiral sampling for instance. Our method thus offers an interesting alternative to spiral imaging, although the instantaneous linear speed of the presented trajectories may not be as high. Indeed, the presence of sharp turns in the SPARKLING trajectory tends to saturate the slew rate while the maximum gradient amplitude is not necessarily reached.

There may be two obstacles to the enhanced performance of the proposed strategy for 2D imaging. First, the modest SNR associated with 2D acquisitions may reduce the effectiveness of our method, as for any other subsampled trajectory. Although our experiments benefited from relatively good SNR conditions owing to a strong magnetic field and the use of a multiple receiver coil, SNR limitations appeared beyond the highest presented in-plane resolution of 390 μm. The second potential limitation is the hardware capacity, namely, the maximum gradient amplitude, the maximum slew rate and the gradient and readout bandwidths, which together control the flexibility and thus, the efficiency of the k-space trajectory. In particular, the gradient raster time plays a critical role and should be as short as possible. Assuming a readout bandwidth larger or equal to the gradient bandwidth, the following practical rule for best SPARKLING use should be observed: the ratio of the number of gradient steps per shot to the image size should be as high as possible. As regards high resolution, long-readout scenarios will maximize this ratio and thus optimize SPARKLING performance, while short-readout acquisitions allow for less departure from simple geometric trajectories. When considering lower resolutions however, our method remains applicable and promising. Moreover, in view of the considerable efforts that are currently being invested to push the hardware limits of gradient systems [66], it is reasonable to expect further improvement of SPARKLING performance.

The SNR limitation should be considerably mitigated by the use of 3D SPARKLING acquisitions, which benefit from improved SNR conditions. Although our demonstration focused on 2D sampling as a proof of concept, the presented method can be extended to 3D imaging, for which further gains in terms of acceleration factors are anticipated. Besides significant concerns about computational efficiency, the 3D extension of the SPARKLING algorithm is straightforward. In this 3D setup, our framework would allow to generate sampling patterns with fully 3D variable density taking advantage of the undersampling potential in all three directions, in contrast to Poisson disk methods which sample along lines in the third direction [67]. Additional improvements may be achieved by incorporating corrections for field inhomogeneities and trajectory deviations into the reconstruction algorithms [68]; these possibilities have yet to be investigated. Most interestingly, in contrast to radial or spiral sampling methods, our technique is able to handle any arbitrary density (e.g., not necessarily radial) and therefore permits the implementation of anisotropic trajectories adapted to organs such as the spinal cord, which may lead to improved image reconstructions [44, 43]. It is worth mentioning that the existing spiral designs are restricted to simple parameterized densities with elliptical level lines [69], which are usually not explicit. SPARKLING can approximate near arbitrary densities.

Our findings may be of value in numerous MRI applications including T_2^* [70, 71], proton-density [72], susceptibility-weighted imaging (SWI) [73] and quantitative susceptibility mapping [74], as our method paves the way to increases in spatial and temporal resolution under conditions compatible with clinical time constraints. Although our application focuses on T_2^* imaging, the SPARKLING trajectories may be used for other contrast such as T_2 or T_1 or for dynamic imaging, by adapting the acquisition parameters. Our framework can also allow to design optimized multi-echo acquisi-

tions, which may be of interest for T_2^*-mapping [75, 76]. By properly adjusting the initialization and target density of the proposed algorithm, any arbitrary sampling trajectory might be improved and potentially replaced. Furthermore, since each segment can be constrained to pass through the origin of the k-space at a given time, our SPARKLING trajectories possess valuable properties such as robustness to motion and potential for self-navigation (e.g., respiratory self-navigation), while remaining efficient. Most interestingly, our method can be readily used for lower magnetic field imaging available in the clinic (3-Tesla) just by adapting the imaging protocol.

ACKNOWLEDGEMENTS

We wish to warmly thank the anonymous reviewers for their excellent work. It allowed us to greatly improve the manuscript along the revision rounds. We would like to express our gratitude to the donors involved in the body donation program of the *Association des dons du corps du Centre Ouest*, Tours, who made this study possible by generously donating their bodies for science. We would like to thank Cyril Poupon for making it possible to use the *ex vivo* phantom. We also wish to thank Françoise Geffroy and Erwan Selingue for their help in manipulating the *ex vivo* phantom. We would like to thank Nicolas Boulant, Vincent Gras and the anonymous referees for their insightful remarks. This research program was supported by a 2016 DRF Impulsion grant (COSMIC, P.I.: P.C.). C.L. was also supported by the CEA international PhD program.

LEGENDS OF SUPPORTING INFORMATION

| Supporting Information Video S1

Video showing the iterations of the SPARKLING algorithm for a uniform target density and an initialization with 32 Cartesian lines as in (Fig. 1a). The multi-scale algorithm was run for 9 decimation levels, during which the number of samples is successively multiplied by two until the final number of samples is reached (3072 samples per shot). Each level comprised 150 iterations. The color of consecutive shots alternates between yellow and blue.

| Supporting Information Video S2

Video showing the iterations of the SPARKLING algorithm for a radially decaying target density and an initialization with 34 symmetric radial segments as in (Fig. 1b). The multi-scale algorithm was run for 6 decimation levels, during which the number of samples is successively multiplied by two until the final number of samples is reached (3072 samples per shot). Each level comprised 150 iterations. The color of consecutive shots alternates between yellow and blue.

| Supporting Information Figure S1

Design of the target density. (Left), The most rapidly vanishing density in the center of the k-space corresponds to the radial trajectories at the maximal speed. (Right), A representative density generated by our algorithm for N=512, $n_c = 34$, $d = 2$, $\tau = 0.5$, $\Delta t = 10\,\mu$s, $\alpha = \frac{\gamma}{2\pi} G_{max}$ and $G_{max} = 40$ mT/m.

| Supporting Information Figure S2

Simulated off-resonance PSF of spiral-initialized and radial-initialized SPARKLING trajectories. Original (left) and simulated off-resonance (right) PSFs of 34-shot SPARKLING trajectories for a spiral initialization (top) or a radial initialization (bottom).

REFERENCES

[1] Barnes J, Bartlett JW, van de Pol LA, Loy CT, Scahill RI, Frost C, et al. A meta-analysis of hippocampal atrophy rates in Alzheimer's disease. Neurobiology of Aging 2009;30(11):1711–1723.

[2] Pruessner J, Li L, Serles W, Pruessner M, Collins D, Kabani N, et al. Volumetry of hippocampus and amygdala with high-resolution MRI and three-dimensional analysis software: minimizing the discrepancies between laboratories. Cerebral Cortex 2000;10(4):433–442.

[3] Van der Kolk AG, Hendrikse J, Zwanenburg JJ, Visser F, Luijten PR. Clinical applications of 7T MRI in the brain. European Journal of Radiology 2013;82(5):708–718.

[4] Duyn JH. The future of ultra-high field MRI and fMRI for study of the human brain. Neuroimage 2012;62(2):1241–1248.

[5] Maclaren J, Armstrong BS, Barrows RT, Danishad K, Ernst T, Foster CL, et al. Measurement and correction of microscopic head motion during magnetic resonance imaging of the brain. PloS One 2012;7(11):e48088.

[6] Federau C, Gallichan D. Motion-correction enabled ultra-high resolution in-vivo 7T-MRI of the brain. PloS one 2016;11(5):e0154974.

[7] Stucht D, Danishad KA, Schulze P, Godenschweger F, Zaitsev M, Speck O. Highest resolution in vivo human brain MRI using prospective motion correction. PloS One 2015;10(7):e0133921.

[8] Vannesjo SJ, Wilm BJ, Duerst Y, Gross S, Brunner DO, Dietrich BE, et al. Retrospective correction of physiological field fluctuations in high-field brain MRI using concurrent field monitoring. Magnetic Resonance in Medicine 2015;73(5):1833–1843.

[9] Pruessmann KP, Weiger M, Scheidegger MB, Boesiger P, et al. SENSE: sensitivity encoding for fast MRI. Magnetic Resonance in Medicine 1999;42(5):952–962.

[10] Griswold MA, Jakob PM, Heidemann RM, Nittka M, Jellus V, Wang J, et al. Generalized autocalibrating partially parallel acquisitions (GRAPPA). Magnetic Resonance in Medicine 2002;47(6):1202–1210.

[11] Candès EJ, Romberg J, Tao T. Robust uncertainty principles: Exact signal reconstruction from highly incomplete frequency information. IEEE Transactions on Information Theory 2006;52(2):489–509.

[12] Donoho DL. Compressed sensing. IEEE Transactions on Information Theory 2006;52(4):1289–1306.

[13] Lustig M, Donoho D, Pauly JM. Sparse MRI: The application of compressed sensing for rapid MR imaging. Magnetic Resonance in Medicine 2007;58(6):1182–1195.

[14] Adcock B, Hansen AC, Poon C, Roman B; Cambridge University Press. Breaking the coherence barrier: A new theory for compressed sensing. Forum of Mathematics, Sigma 2017;5.

[15] Boyer C, Chauffert N, Ciuciu P, Kahn J, Weiss P. On the generation of sampling schemes for Magnetic Resonance Imaging. SIAM Journal on Imaging Sciences 2016;9(4):2039–2072.

[16] Dippé MA, Wold EH. Antialiasing through stochastic sampling. ACM Siggraph Computer Graphics 1985;19(3):69–78.

[17] De Goes F, Breeden K, Ostromoukhov V, Desbrun M. Blue noise through optimal transport. ACM Transactions on Graphics (TOG) 2012;31(6):171.

[18] Edelstein WA, Hutchison JM, Johnson G, Redpath T. Spin warp NMR imaging and applications to human whole-body imaging. Physics in Medicine and Biology 1980;25(4):751.

[19] Mansfield P. Multi-planar image formation using NMR spin echoes. Journal of Physics C: Solid State Physics 1977;10(3):L55.

[20] Lauterbur PC. Image formation by induced local interactions: examples employing nuclear magnetic resonance. Nature 1973;242(190).

[21] Bergin C, Pauly J, Macovski A. Lung parenchyma: projection reconstruction MR imaging. Radiology 1991;179(3):777–781.

[22] Glover G, Pauly J. Projection reconstruction techniques for reduction of motion effects in MRI. Magnetic Resonance in Medicine 1992;28(2):275–289.

[23] Ahn C, Kim J, Cho Z. High-speed spiral-scan echo planar NMR imaging-I. IEEE Transactions on Medical Imaging 1986;5(1):2–7.

[24] Meyer CH, Hu BS, Nishimura DG, Macovski A. Fast spiral coronary artery imaging. Magnetic Resonance in Medicine 1992;28(2):202–213.

[25] Pipe JG, et al. Motion correction with PROPELLER MRI: application to head motion and free-breathing cardiac imaging. Magnetic Resonance in Medicine 1999;42(5):963–969.

[26] Jackson JI, Nishimura DG, Macovski A. Twisting radial lines with application to robust magnetic resonance imaging of irregular flow. Magnetic Resonance in Medicine 1992;25(1):128–139.

[27] Bilgin A, Trouard T, Gmitro A, Altbach M. Randomly perturbed radial trajectories for compressed sensing MRI. In: Proceedings of the 16th annual meeting of ISMRM Toronto, Canada; 2008. p. 3152.

[28] Lustig M, Lee JH, Donoho DL, Pauly JM. Faster imaging with randomly perturbed, under-sampled spirals and ℓ_1 reconstruction. In: Proceedings of the 13th annual meeting of ISMRM Miami Beach, FL, USA; 2005. p. 685.

[29] Wang H, Wang X, Zhou Y, Chang Y, Wang Y. Smoothed random-like trajectory for compressed sensing MRI. In: Engineering in Medicine and Biology Society (EMBC), 2012 Annual International Conference of the IEEE IEEE; 2012. p. 404–407.

[30] Barzilai J, Borwein JM. Two-point step size gradient methods. IMA journal of Numerical Analysis 1988;8(1):141–148.

[31] Tan H, Meyer CH. Estimation of k-space trajectories in spiral MRI. Magnetic Resonance in Medicine 2009;61(6):1396–1404.

[32] Lazarus C, Marz M, Weiss P. Correcting the side effects of ADC filtering in MR image reconstruction. preprint 2018;.

[33] Chauffert N, Weiss P, Kahn J, Ciuciu P. A projection algorithm for gradient waveforms design in Magnetic Resonance Imaging. IEEE Transactions on Medical Imaging 2016 Sep;35(9):2026–2039.

[34] Chauffert N, Ciuciu P, Kahn J, Weiss P. A projection method on measures sets. Constructive Approximation 2017;45(1):83–111.

[35] Schmaltz C, Gwosdek P, Bruhn A, Weickert J. Electrostatic halftoning. In: Computer Graphics Forum, vol. 29 Wiley Online Library; 2010. p. 2313–2327.

[36] Cline HE, Zong X, Gai N. Design of a logarithmic k-space spiral trajectory. Magnetic Resonance in Medicine 2001;46(6):1130–1135.

[37] Daubechies I, DeVore R. Approximating a bandlimited function using very coarsely quantized data: A family of stable sigma-delta modulators of arbitrary order. Annals of mathematics 2003;158(2):679–710.

[38] Bernstein MA, King KF, Zhou XJ. Handbook of MRI pulse sequences.; 2004.

[39] Jouda M, Gruschke OG, Korvink JG. A new fully integrated multichannel receiver design for magnetic resonance imaging. Concepts in Magnetic Resonance Part B: Magnetic Resonance Engineering 2016;46(3):134–145.

[40] Ansorge R, Graves MJ. The Physics and Mathematics of MRI. Morgan & Claypool Publishers; 2016.

[41] Chauffert N, Ciuciu P, Kahn J, Weiss P. Variable density sampling with continuous trajectories. SIAM Journal on Imaging Sciences 2014;7(4):1962–1992.

[42] Zhang Y, Dragotti P. On the Reconstruction of Wavelet-Sparse Signals From Partial Fourier Information. IEEE Signal Processing Letters 2015;22:1234–1238. http://dx.doi.org/10.1109/LSP.2015.2393953.

[43] Gözcü B, Mahabadi RK, Li YH, Ilıcak E, Cukur T, Scarlett J, et al. Learning-Based Compressive MRI. IEEE Transactions on Medical Imaging 2018;37(6):1394–1406.

[44] Kutyniok G, Lim WQ. Optimal compressive imaging of fourier data. SIAM Journal on Imaging Sciences 2018;11(1):507–546.

[45] Mainero C, Benner T, Radding A, Van Der Kouwe A, Jensen R, Rosen B, et al. In vivo imaging of cortical pathology in multiple sclerosis using ultra-high field MRI. Neurology 2009;73(12):941–948.

[46] Nayak KS, Nishimura DG. Randomized trajectories for reduced aliasing artifact. In: Proceedings of the 6th Annual Meeting of ISMRM Sydney, Australia; 1998. p. 670.

[47] Tsai CM, Nishimura DG. Reduced aliasing artifacts using variable-density *k*-space sampling trajectories. Magnetic Resonance in Medicine 2000;43(3):452–458.

[48] Smith TB, Nayak KS. MRI artifacts and correction strategies. Imaging in Medicine 2010;2(4):445–457.

[49] Jezzard P, Clare S, et al. Sources of distortion in functional MRI data. Human Brain Mapping 1999;8(2-3):80–85.

[50] Lee JH, Hargreaves BA, Hu BS, Nishimura DG. Fast 3D imaging using variable-density spiral trajectories with applications to limb perfusion. Magnetic Resonance in Medicine 2003;50(6):1276–1285.

[51] Law CS, Glover GH. Interleaved spiral-in/out with application to functional MRI (fMRI). Magnetic Resonance in Medicine 2009;62(3):829–834.

[52] Wu B, Millane R, Watts R, Bones P. Applying compressed sensing in parallel MRI. In: Proceedings of the 16th Annual Meeting of ISMRM, vol. 1480 Toronto, Canada; 2008. .

[53] Liu B, Zou YM, Ying L. SparseSENSE: application of compressed sensing in parallel MRI. In: Information Technology and Applications in Biomedicine, 2008. ITAB 2008. International Conference on IEEE; 2008. p. 127–130.

[54] Boyer C, Ciuciu P, Weiss P, Mériaux S. HYR^{2}PICS: Hybrid regularized reconstruction for combined parallel imaging and compressive sensing in MRI. In: Biomedical Imaging (ISBI), 2012 9th IEEE International Symposium on IEEE; 2012. p. 66–69.

[55] Keiner J, Kunis S, Potts D. Using NFFT 3—a software library for various nonequispaced fast Fourier transforms. ACM Transactions on Mathematical Software (TOMS) 2009;36(4):19.

[56] Shin PJ, Larson PE, Ohliger MA, Elad M, Pauly JM, Vigneron DB, et al. Calibrationless parallel imaging reconstruction based on structured low-rank matrix completion. Magnetic Resonance in Medicine 2014;72(4):959–970.

[57] Uecker M, Hohage T, Block KT, Frahm J. Image reconstruction by regularized nonlinear inversion-joint estimation of coil sensitivities and image content. Magnetic Resonance in Medicine 2008;60(3):674–682.

[58] Yeh EN, Stuber M, McKenzie CA, Botnar RM, Leiner T, Ohliger MA, et al. Inherently self-calibrating non-Cartesian parallel imaging. Magnetic Resonance in Medicine 2005;54(1):1–8.

[59] Taylor AB, Hendrickx JM, Glineur F. Exact worst-case convergence rates of the proximal gradient method for composite convex minimization. preprint arXiv:170504398 2017;.

[60] Vannesjo SJ, Haeberlin M, Kasper L, Pavan M, Wilm BJ, Barmet C, et al. Gradient system characterization by impulse response measurements with a dynamic field camera. Magnetic Resonance in Medicine 2013;69(2):583–593.

[61] De Zanche N, Barmet C, Nordmeyer-Massner JA, Pruessmann KP. NMR probes for measuring magnetic fields and field dynamics in MR systems. Magnetic Resonance in Medicine 2008;60(1):176–186.

[62] Lustig M, Donoho DL, Santos JM, Pauly JM. Compressed sensing MRI. IEEE Signal Processing Magazine 2008;25(2):72–82.

[63] Yudilevich E, Stark H. Spiral sampling in magnetic resonance imaging-the effect of inhomogeneities. IEEE Transactions on Medical Imaging 1987;6(4):337–345.

[64] Mason GF, Harshbarger T, Hetherington HP, Zhang Y, Pohost GM, Twieg DB. A Method to measure arbitrary k-space trajectories for rapid MR imaging. Magnetic Resonance in Medicine 1997;38(3):492–496.

[65] Börnert P, Schomberg H, Aldefeld B, Groen J. Improvements in spiral MR imaging. Magnetic Resonance Materials in Physics, Biology and Medicine 1999;9(1):29–41.

[66] Weiger M, Overweg J, Rösler MB, Froidevaux R, Hennel F, Wilm BJ, et al. A high-performance gradient insert for rapid and short-T2 imaging at full duty cycle. Magnetic Resonance in Medicine 2018;79(6):3256–3266.

[67] Vasanawala SS, Alley MT, Hargreaves BA, Barth RA, Pauly JM, Lustig M. Improved pediatric MR imaging with compressed sensing. Radiology 2010;256(2):607–616.

[68] Sutton BP, Noll DC, Fessler JA. Fast, iterative image reconstruction for MRI in the presence of field inhomogeneities. IEEE transactions on Medical Imaging 2003;22(2):178–188.

[69] King KF. Spiral scanning with anisotropic field of view. Magnetic Resonance in Medicine 1998;39(3):448–456.

[70] Frischer JM, Göd S, Gruber A, Saringer W, Grabner G, Gatterbauer B, et al. Susceptibility-weighted imaging at 7 T: improved diagnosis of cerebral cavernous malformations and associated developmental venous anomalies. NeuroImage: Clinical 2012;1(1):116–120.

[71] De Guio F, Vignaud A, Ropele S, Duering M, Duchesnay E, Chabriat H, et al. Loss of venous integrity in cerebral small vessel disease: a 7-T MRI study in cerebral autosomal-dominant arteriopathy with subcortical infarcts and leukoencephalopathy (CADASIL). Stroke 2014;45(7):2124–2126.

[72] Kasper L, Engel M, Barmet C, Haeberlin M, Wilm BJ, Dietrich BE, et al. Rapid anatomical brain imaging using spiral acquisition and an expanded signal model. NeuroImage 2017;.

[73] Haacke EM, Xu Y, Cheng YCN, Reichenbach JR. Susceptibility weighted imaging (SWI). Magnetic Resonance in Medicine 2004;52(3):612–618.

[74] Langkammer C, Bredies K, Poser BA, Barth M, Reishofer G, Fan AP, et al. Fast quantitative susceptibility mapping using 3D EPI and total generalized variation. Neuroimage 2015;111:622–630.

[75] Bittersohl B, Hosalkar HS, Hughes T, Kim YJ, Werlen S, Siebenrock KA, et al. Feasibility of T 2* mapping for the evaluation of hip joint cartilage at 1.5 T using a three-dimensional (3D), gradient-echo (GRE) sequence: A prospective study. Magnetic Resonance in Medicine 2009;62(4):896–901.

[76] Denk C, Rauscher A. Susceptibility weighted imaging with multiple echoes. Journal of Magnetic Resonance Imaging 2010;31(1):185–191.